Structural insights into the vapochromic behavior of Pt- and Pd-based compounds

Benny Danilo Belviso,[1] Francesco Marin,[2] Sara Fuertes,[3] Violeta Sicilia,[3] Rosanna Rizzi,[1] Fulvio Ciriaco,[5] Chiara Cappuccino,[2] Eric Dooryhee,[4] Aurelia Falcicchio,[1] Lucia Maini,[2] Angela Altomare[1] and Rocco Caliandro[1,]*

1 Institute of Crystallography, CNR, via Amendola 122/o, Bari, 70126, Italy.
2 Dipartimento di Chimica "Giacomo Ciamician", Università di Bologna Via Selmi 2, 40126, Bologna, Italy.
3 Departamento de Química Iorgánica, Universidad de Zaragoza-CSIC, Zaragoza, Spain.
4 NSLS II, Photon Science Division, Brookhaven National Laboratory, New York.
5 Dipartimento di Chimica, Università di Bari, via Orabona, 70125, Bari, Italy.

Abstract Anionic complexes having vapochromic behavior are investigated: $[K(H_2O)][M(ppy)(CN)_2]$, $[K(H_2O)][M(bzq)(CN)_2]$ and $[Li(H_2O)_n][Pt(bzq)(CN)_2]$ where ppy=2-phenylpyridinate and bzq=7,8-benzoquinolate and M=Pt(II) or Pd(II). These hydrated potassium/lithium salts exhibit a change in color upon heating to 110° C, and they transform back into the original color upon absorption of water molecules from the environment. These compounds were characterized by using thermogravimetric analysis to investigate the dehydration process, and high-resolution X-ray-based measurements to gain static and dynamical structural information. Single crystals were used to determine the crystal structure of the compounds in their initial state, while powder samples were used to investigate the kinetics of the structural changes induced by temperature variations. X-ray absorption spectroscopy and X-ray diffraction with pair distribution function setup allowed studying the local structure even in samples lacking long-range order. The main trends in data were promptly extracted without any prior knowledge on the static crystal structure of the compounds by a multivariate approach, while structural refinement against individual profiles was attempted for compounds with higher crystallinity. Order parameters of the vapochromic transition were determined, as derived by principal component analysis and crystallinity estimations, and the kinetic model best describing the transition, together with its kinetics parameters, was determined for each of the compounds. The challenging task of determining the structural changes involved in the vapochromic transition even in the presence of partially ordered and impure crystalline material has been tackled by pushing the limits of X-ray data analysis.

1. Introduction

Vapochromic materials can detect volatile organic compounds (VOCs) below the ppm level. Of particular interest are stimuli-responsible compounds that show dramatic and reversible color changes

upon exposure to VOCs. They allow detection of VOCs even by the naked eye as an effect of structural changes in the solid state, triggered by vapor uptake. These properties are typically showed by metal compounds such as Pt(II)- or Pd(II)- containing cyclometalated complexes, which can be assembled by using coordination polymerization reactions and by tuning the bond strength with an appropriate assembly of metal ions and coordinating Pt(II) and Pd(II) metalloligands [1,2,3,4]. Coordination polymers $[K(H_2O)][M(ppy)(CN)_2]$ and $[K(H_2O)][M(bzq)(CN)_2]$, with ppy=2-phenylpyridinate, bzq=7,8-benzoquinolate, and M=Pt or Pd (Figure 1), are examples of anionic complexes exhibiting vapochromism. Upon heating to 110° C, these compounds lose the crystal water and experience a change in color from red or purple to yellow (Pt) or from yellow to white (Pd). When the anhydrous species are exposed to air, they undergo inverse changes of color within seconds due to water-molecules uptake. The origin of this vapochromic behavior is thought to be related to the altered metallophilic M-M interactions upon solvent absorption. However, so far only the $[K(H_2O)][Pt(ppy)(CN)_2]$ precursor complex has been structurally characterized [5] and in-depth investigations of the structural changes related to the vapochromic transition were never attempted. A preliminary characterization of the vapochromic behavior of compounds $[K(H_2O)][Pt(bzq)(CN)_2]$ and $[K(H_2O)][Pt(ppy)(CN)_2]$ by X-ray diffraction is reported in [6].

In this study, the structural features of the four compounds are investigated. In addition $[Li(H_2O)_n][Pt(bzq)(CN)_2]$ is also examined to evaluate the influence of the counterion. Their vapochromic transition is characterized in the solid state by using high-resolution X-ray measurements. X-ray absorption spectroscopy and pair distribution function are used to study short-range changes, while X-ray diffraction is used to investigate the long-range order. Besides static measurements, aimed at determining the crystal packing and the 3D atomic arrangement, *in situ* measurements are performed while varying the temperature on the sample, to investigate the structural dynamics underlying the vapochromic transition. The large amount of data collected has been first processed by multivariate analysis, to capture main trends in data without any a priori structural knowledge. Then individual profiles have been structurally interpreted for compounds showing the highest crystalline order. Further insight into the dehydration process was gained using thermogravimetric analysis (TGA).

Ab initio phasing methods from single-crystal data and direct space methods based on simulated annealing [7] from X-ray powder diffraction (XRPD) data, coupled with DFT calculations and PDF refinements, allow to obtain static structural models of the compounds in their initial and final states. The structural information obtained provides further insight into strategies to achieve engineered vapochromic complexes, which selectively and rapidly respond to specific vapors in small quantities.

2. Materials and Methods

2.1. Sample preparation

Compounds considered in this study are summarized in Table 1. Vapochromic transitions manifest themselves with dramatic color changes and can be achieved by heating the samples or putting them in vacuum. Reverse transitions are obtained by allowing water molecules in the air to interact with the powder sample. The ppy/bzq ligands (Figure 1) exhibit a very similar structure, with only two added carbon atoms present in bzq, which complete a third aromatic ring.

2.1.1 Compounds Pt(ppy)K and Pt(bzq)K

Compounds Pt(ppy)K and Pt(bzq)K were prepared according to what is reported in Forniés *et al.*, [5], and characterized by IR, 1H NMR and UV-vis spectroscopy. Especially significant is the presence in their IR spectra of two νCN absorptions around 2100 cm^{-1} and 2120 cm^{-1}, corresponding to two terminal CN ligands in a cis arrangement and a strong absorption at 3400 cm^{-1} indicative of the presence of water in the solid [5]. The amount of water can be determined from their 1H NMR spectra in non-water containing acetone-d6. In addition to the signals corresponding to the bzq or ppy group, one signal at about 2.9 ppm is assigned to one molecule of water [5].

The UV-vis. spectra in the solid state show intense absorptions at λ < 450 nm assigned to IL/MLCT transitions and further absorption maxima at λ = 564 nm and 548 nm for Pt(ppy)K and Pt(bzq)K, respectively [5]. These latter are assigned to metal-metal-to-ligand charge transfer ^{1}MMLCT [dσ*(Pt) → π*(bzq/ppy)] transitions, and are responsible for the intense color showed by these compounds; they are also considered the fingerprint of the existence of short Pt - Pt contacts (3.0-3.5 Å), since stronger M-M interactions lead to shorter M-M distance and lower energy absorption. Upon heating in the oven at 110° C, the lowest energy absorption band assigned to the ^{1}MMLCT transitions disappears from UV-vis spectra, which evidences the profound structural changes operating in the solids by the loss of the water molecules.

2.1.2 Compounds Pd(ppy)K, Pd(bzq)K and Pt(bzq)Li

[Pd(bzq)(NCMe)$_2$]ClO$_4$ [8], [Pd(ppy)(NCMe)$_2$]ClO$_4$ [8] and NBu$_4$[Pt(bzq)(CN)$_2$] [5] were prepared according to the literature procedures.

Synthesis of Pd(bzq)K: KCN (70.0 mg, 1.075 mmol) was added to a stirred suspension of [Pd(bzq)(NCMe)$_2$]ClO$_4$ (250.0 mg, 0.536 mmol) in MeOH (60 mL) at rt. After 1h the mixture was concentrated to 10 mL, kept at −30ºC for 2 h, and filtered through celite. The resulting solution was evaporated to dryness and diethyl ether (20 mL) was added to the residue to give a yellow solid. Yield: 161.0 mg, 76%. IR: $\tilde{\nu}$ (cm^{-1}): 3499, 3390 (vs, H$_2$O), 2123(vs, C≡N), 2112 (vs, C≡N). 1624 (m, H$_2$O), 1570 (m), 823 (vs), 815 (vs), 749 (s). Negative FAB-MS (m/z): 336 [Pd(bzq)(CN)$_2$]$^-$. ^{1}H NMR (acetone-d_6, 300 MHz, δ (ppm), *J* (Hz)) δ: 9.37 (dd, H$_2$, $^3J_{H2-H3}$ = 5.1, $^4J_{H2-H4}$ = 1.5), 8.53 (dd, H$_4$, $^3J_{H4-H3}$ = 8.0, $^4J_{H4-H2}$ = 1.5), 8.20 (d, H$_9$, $^3J_{H9-H8}$ = 7.0), 7.82 (H$_5$, ν$_A$), 7.71 (H$_6$, ν$_B$, $^3J_{H5-H6}$ = 8.7), 7.69 (dd, H$_3$, $^3J_{H3-H4}$ = 8.1, $^4J_{H3-H2}$ = 5.1, H$_3$), 7.60 (d, H$_7$, $^3J_{H7-H8}$ = 8.0), 7.45 (t, H$_8$, $^3J_{H-H}$ = 7.0).

Synthesis of Pd(ppy)K: It was prepared following the same method for [K(H$_2$O)][Pd(bzq)(CN)$_2$]. KCN (56.5 mg, 0.868 mmol) and [Pd(ppy)(NCMe)$_2$]ClO$_4$ (192.0 mg, 0.434 mmol). Yield: 129.1 mg, 80%. IR: $\tilde{\nu}$ (cm^{-1}): 3466 (vs, H$_2$O), 2115(vs, C≡N), 2104 (vs, C≡N). 1630 (m, H$_2$O), 1606 (s), 1582 (m), 785 (vs), 743 (vs). Negative FAB-MS (m/z): 312 [Pd(ppy)(CN)$_2$]$^-$. ^{1}H NMR (acetone-d_6, 300 MHz, δ (ppm), *J* (Hz)) δ: 9.15 (d, H$_2$, $^3J_{H2-H3}$ = 5.1), 8.05 (m, H$_9$), [8.00-7.90] (m, 2H, H$_4$, H$_5$), 7.61 (m, H$_6$), 7.29 (t, H$_3$, $^3J_{H-H}$= 6.1), [6.97-7.05] (m, 2 H, H$_7$, H$_8$).

Synthesis of Pt(bzq)Li: LiBr (78.1 mg, 0.898 mmol) was added to a yellow solution of NBu$_4$[Pt(bzq)(CN)$_2$] (600.0 mg, 0.897 mmol) in anhydrous MeOH (20 mL) at r. t.. After stirring the reaction mixture for 4h under Ar atmosphere, the resulting solution was evaporated to dryness. The residue was treated with three fractions of CH$_2$Cl$_2$ (5 mL) and evaporated to dryness after each addition. Then, 20 mL of CH$_2$Cl$_2$ were added and the resulting solid was filtered. The solid was recrystallized with acetone (30 mL) / CH$_2$Cl$_2$ (20 mL) to give a yellow solid. Yield: 356.6 mg, 78% (n = 4). IR: $\tilde{\nu}$ (cm^{-1}): 3380 (vs, H$_2$O), 2131(vs, C≡N), 2105 (vs, C≡N). 1636 (m, H$_2$O), 1619 (s), 822 (vs), 816 (vs), 749 (s). Negative FAB-MS (m/z): 425 [Pt(bzq)(CN)$_2$]$^-$. ^{1}H NMR (293K, acetone-d_6, 400 MHz, δ (ppm), *J* (Hz)) δ: 9.60 (dd, H$_2$, $^3J_{H2-H3}$ = 5.2, $^4J_{H2-H4}$ = 1.6, $^3J_{Pt-H2}$ = 32.0), 8.60 (dd, H$_4$, $^3J_{H4-H3}$ = 8.0, $^4J_{H4-H2}$ = 1.4), 8.23 (dd, H$_9$, $^3J_{H9-H8}$ = 7.0, $^4J_{H9-H7}$ = 1.2, $^3J_{Pt-H9}$ = 46.0), 7.84 (H$_5$, ν$_A$), 7.70 (H$_6$, ν$_B$, $^3J_{H5-}$

$_{H6}$ = 8.8), 7.72 (dd, H$_3$, $^3J_{H3\text{-}H4}$ = 8.0, $^3J_{H3\text{-}H2}$ = 5.2), 7.62 (dd, H$_7$, $^3J_{H7\text{-}H8}$ = 8.0, $^4J_{H7\text{-}H9}$ = 1.2), 7.50 (dd, H$_8$, $^3J_{H8\text{-}H7}$ = 8.0, $^3J_{H8\text{-}H9}$ = 7.0).

The UV-vis. spectra in the solid state are shown in Figure S1. The lowest energy absorptions assigned to the [1]MMLCT transitions have maxima at λ ~ 420 nm for the hydrated Pd(ppy)K and Pd(bzq)K, and at ~ 550 nm for Pt(bzq)Li, appearing just as a shoulder in the two later ones. These facts are in agreement with the yellow color of the powdered samples, and indicate less significant variation of M-M interactions between hydrated and anhydrous forms of Pd(bzq)K and Pt(bzq)Li.

The amount of water molecules determined from 1H NMR is 1 for Pd(bzq)K and Pd(ppy)K (Figures S2, S3), and 4 for Pt(bzq)Li (Figure S4). This latter determination is in agreement with elemental analysis: CHN Analysis calculated for $C_{15}H_{16}LiN_3O_4Pt$ (%): C, 35.72; H, 3.20; N, 8.33. Found: 35.74; H, 2.93; N, 8.16.

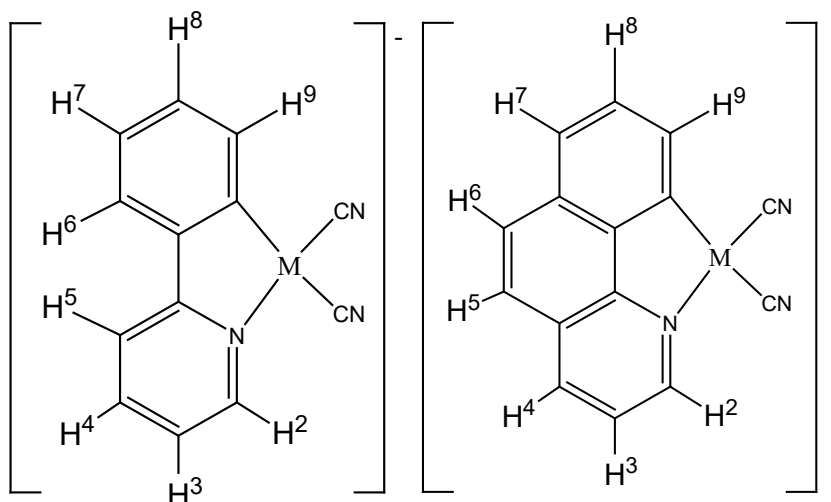**Figure 1**. Scheme of the two ligands of metal ion M=Pt/Pd considered in this study. Numerical scheme for NMR purposes.

Table 1. Compounds considered in this study.

Formula	Short name
[K(H$_2$O)][Pt(bzq)(CN)$_2$]	Pt(bzq)K
[K(H$_2$O)][Pt(ppy)(CN)$_2$]	Pt(ppy)K
[K(H$_2$O)][Pd(bzq)(CN)$_2$]	Pd(bzq)K
[K(H$_2$O)][Pd(ppy)(CN)$_2$]	Pd(ppy)K
[Li(H$_2$O)$_n$][Pt(bzq)(CN)$_2$]	Pt(bzq)Li

bzq = 7,8-benzoquinolate

ppy = 2-phenylpyridinate

2.2. Thermogravimetric analysis

Thermogravimetric measurements were performed using a Perkin Elmer TGA7 in the temperature range 35-300° C under N_2 gas flow. Heating was carried out at 5° C min^{-1}.

2.3. X-ray absorption spectroscopy

XAS measurements were performed at the European Synchrotron Radiation Facility (ESRF), beamline ID26 on compound Pt(bzq)K. Two capillaries filled by powder sample were attached to a sample holder, one of them was heated to 100° C before being sealed (Figure S22a). To reduce photodegradation, successive measurements of a few seconds were performed within liquid He by shifting the sample in the primary X-ray. Data analysis was performed by using the program ATHENA and ARTEMIS [9]. The signal-to-noise ratio was improved by merging four to eight scans of the same sample. Small energy shifts between scans of the same sample were corrected with the ATHENA alignment procedure.

2.4. Static powder X-ray diffraction

X-ray powder diffractions were collected at room temperature using Panalytical X'Pert PRO diffractometer operating at 40 kV and 40 mA, equipped with a focusing mirror and a Pixel detector. Measurements were executed in transmission mode, by placing the sample in a 0.3 mm glass capillary, and by using Cu–K□ radiation (λ = 1.54056 Å) without a monochromator. The angular range 3-85° (2ϑ) was spanned with a step size of 0.013° and a time/step of 200 s. In order to reduce possible preferred orientation effects, the capillary was rotated during measurement to improve the randomization of individual crystallites orientations. Qualitative analysis by powder diffraction data of Pt(ppy)K collected at room temperature was executed by QUALX2.0 software using the POW_COD database [10]. Structure solution by powder diffraction data of Pd(ppy)K collected at room temperature was carried out by the EXPO2014 software [11].

2.5. Single-crystal X-ray diffraction

Diffraction data from a single crystal of Pt(ppy)K were collected at room temperature on an Oxford Xcalibur S instrument with Mo–Kα radiation (λ = 0.71073 Å) and a graphite monochromator. Data were reduced with the Rigaku CrysAlisPro program [12]. Absorption correction was done by the multi-scan method using the SCALE3 ABSPACK scaling algorithm. SIR2019 [13] was used for structure solution and SHELXL [14] for the refinement based on F^2. The non-hydrogen atoms were treated anisotropically. The O-bounded H atoms (H2a and H2b) that are responsible for water bonding to the framework were pre-located at calculated positions and constrained to a bond distance of 0.947 Å. The other hydrogen atoms were refined using a riding model with d(C–H) = 0.99 Å and Uiso(H) = 1.2 Ueq(C) for –CH– hydrogen atoms. The Mercury software package [15] and Ortep program [16] were used to prepare molecular graphics and materials for publication.

2.6. In situ powder X-ray diffraction

Variable temperature X-ray powder diffraction (VTXRPD) analyses were performed on a PANalytical X'Pert Pro automated diffractometer with an X'Celerator detector in Bragg–Brentano geometry, using Cu–Kα radiation (λ = 1.5418 Å) without monochromator in the 2ϑ range between 3.5° and 40.0° (continuous scan mode, step size 0.0167°, counting time 19.685 s, Soller slit 0.04 rad, antiscatter slit 0.76 mm, divergence slit 0.38 mm, 40 mA x 40 kV) equipped with an Anton Paar TTK 450 system for measurements at a controlled temperature.

2.7. In situ pair distribution function

X-ray data were collected at the X17A beamline of the National Synchrotron Light Source (NSLS) of the Brookhaven National Laboratory with an X-ray energy of 66.7 keV (0.18597 Å) and a 0.5 mm x 0.5 mm beam size. A Perkin Elmer large area detector (2048 x 2048 pixels and 200 x 200 μm pixel size) was mounted orthogonal to the beam path, 202 mm downstream from the sample. Lanthanum hexaboride (LaB6) was measured as a standard material to calibrate the detector geometry, including the sample-to-detector distance. The temperature was first increased from 20° C to 150° C and then decreased to 20° C by using a cryo-cooler. A step of 5° C was done every 10 minutes, during which a complete measurement and a monochromator realignment were automatically performed. Each data collection lasted about 2 minutes, and in the remaining 8 minutes the X-ray shutter was closed to avoid radiation damage of the sample. An empty capillary was measured for background estimation. Diffraction images data were azimuthally integrated and converted into intensity profiles versus 2ϑ and versus momentum transfer $Q = 4\pi \sin \vartheta / \lambda$ by using the FIT2D program [17]. PDF profiles were calculated up to interatomic distances r of 40 Å from the Q profiles by the program PDFGetX3 [18]. The parameters for PDF calculation (background subtraction scale factor, minimum and maximum values of Q, degree of data-correction polynomial) were optimized on individual PDF profiles, such as to avoid large termination effects and to preserve the signal to noise ratio. A different setting of parameter was chosen when calculating PDF profiles for multivariate analysis. In this case, the parameters were kept constant among the profiles of the same compound, as they are all processed at the same time.

PDF data were refined against the crystal structure solution of the same compound determined by single-crystal X-ray diffraction in the case of the Pt(ppy)K compound. For the other compounds, the initial model was obtained by properly modifying the metal atom and the ligand, keeping constant the crystal symmetry and the position of the molecule in the crystal cell. Individual profiles were refined independently, starting from that collected at room temperature, by using the program DiffPy-CMI [19]. The fit has been executed for interatomic distances comprised between 1.5 Å and 28 Å, to avoid finite-size artifacts in the low r range and to reduce noise contribution in the high r range. As a first step of the refinement procedure, the following parameters are refined separately, i.e. by keeping constant all the others: scale factor, free lattice parameters, position and orientation of the molecule, atomic displacement parameters and peak shape parameters *broad,* (peak broadening from increased intensity noise at high Q) and *delta1* (coefficient for $1/r$ contribution to the peak sharpening). As a second step, atomic positions are varied, with bond lengths, angles and torsions restrained during the fitting. The refined structure obtained from a given profile, together with the scale factor and *broad* and *delta1* parameters, is used as the starting model to the next profile.

2.8. Multivariate analysis of X-ray diffraction data

Time-dependent PDF profiles were processed by the program RootProf [20] to perform qualitative analysis through principal component analysis (PCA). It is a projection method [21], which can be used to reduce the dimensionality of the data set constituted by the measured profiles. Principal components (PCs) are calculated as eigenvectors of the covariance matrix of the data, whose eigenvalues represent the variance of the data along the eigenvector directions. The initial dimensionality of the data set, equal to the number of 2ϑ values used to describe the diffraction profiles, is reduced to a small number (typically 2) of PCs used to describe the data. Score and loading vectors are two alternative representations of the data matrix: the former carries information about samples (measurements) in variable 2ϑ space, the latter about variables in crystal space.

2.9. Crystallinity and average crystallite size

The crystallinity fraction in the XRPD profiles has been determined in the 2ϑ range between 7° and 31°, which includes the highest peaks in the profiles. It has been calculated as the area above the background divided by the total area under the diffraction peaks, where the background was estimated by using the SNIP algorithm [22]. The average crystallite size has been estimated by fitting the highest peak in the XRPD profiles with a pseudo-Voigt function and by using the Scherrer equation [23]. The highest peak is located at nearly the same angular position for all compounds (2ϑ=10.0° for Pt(bzq)Li, 2ϑ=9.9 for the others), and represents diffraction from the family of planes (102) for Pt(ppy)K and Pd(ppy)K. Structure is assumed to be essentially strain-free. The LaB6 standard was used to estimate the instrumental peak broadening. All calculations have been performed by the RootProf program [20].

2.10. Kinetic analysis

When PCA is applied to *in situ* XRPD or PDF data, the scores of the first principal component (PC1) capture the main trend in data as a function of the temperature. Thus they can be considered as a reaction coordinate, i.e. an abstract one-dimensional coordinate that represents progress along a reaction pathway. A kinetic analysis has been applied to the reaction coordinate by using the algorithms described in [24] and included in the RootProf program [20]. In brief, the kinetic equation

$$\frac{d\alpha}{dt} = f(\alpha) \cdot A \cdot exp\left(-\frac{E_a}{RT}\right) \qquad (1)$$

is approximated by the Coats and Redfern-Coats equation [25]:

$$\log\left(\frac{g(\alpha)}{T^2}\right) = \log A - \frac{E_a}{RT} \cdot \qquad (2)$$

where α is the reaction coordinate, *f(α)* and $g(\alpha) = \int_0^\alpha \frac{d\alpha}{f(\alpha)}$ are functions describing the kinetic model, *T* is the temperature in Kelvin, *R* is the universal gas constant, *A* is the frequency factor and E_a is the activation energy. The frequency factor can be interpreted as the frequency of molecules that collide in the correct orientation and with enough energy to initiate the reaction, while the activation energy is the threshold energy that the reactant(s) must acquire before reaching the transition state. The best kinetic model describing the data is selected among those commonly used for solid-state

reactions by using the Masterplot technique [26]. The formula of $g(\alpha)$ for the Avrami-Eroféev kinetic model is [26]:

$$g(\alpha) = [-ln(1-\alpha)]^{1/n} \qquad (3)$$

where n is the parameter defining the reaction order. It is determined by a fitting procedure based on the Materplot technique [24]. The parameters A and E_a are then determined by fitting data with eq. (2), with the function $g(\alpha)$ identified by the selected kinetic model.

3. Results and discussion

3.1. Single-crystal structure solution

Recrystallization experiments were attempted aiming at growing larger crystals of all compounds. Crystals with dimensions suitable for single-crystal X-ray diffraction experiments (>50 µm) were obtained only for Pt(ppy)K. The summary of the crystallographic data and structure refinement details for this compound are given in Table 2.

Table 2 Crystallographic data and structure refinement details for Pt(ppy)K.

Empirical Formula	$C_{13}H_{10}KN_3OPt$
Formula Weight	458.43
Temperature (K)	293
Crystal system	orthorhombic
Space group	*Pbca*
a (Å)	9.9886 (5)
b (Å)	6.7941 (4)
c (Å)	38.6467 (4)
Volume (Å^3)	2622.7 (2)
Z	8
ρ_{calc} (g/cm^3)	2.322
μ (mm^{-1})	11.01
F(000)	1712
Crystal size (mm^3)	0.0002567
Radiation	Cu
Reflections collected	3231
Independent reflections	1972
Data/restraints/parameters	1972/8/172
Final R indexes [$I > 2\sigma(I)$]	0.1087
Final R indexes [all data]	0.1613
Highest difference peak/hole (eÅ^{-3})	6.497/-4.001

The evidence of the space group was not immediate: two plausible solutions were obtained in *Pca*2$_1$ and *Pbca*, respectively. The space group of Pt(ppy)K was assessed by DFT calculations (see §3.1.1).

The structure solution and refinement processes were carried out with difficulties, providing questionable results. The use of restraints on bond lengths (C20-C11, C11-C2, C13-C11, C18-C13, C24-C21, C18-C21, O2-H2A, O2-H2B), in the refinement process, was necessary for reaching the convergence. The refined structure has a high residual electron density outside the metal ion location;

the highest difference peak and the deepest hole are 6.497 and -4.001 eÅ^{-3}, respectively. Attempts to account for possible model errors were considered, but they did not improve the refinement process. The poor quality of diffraction data could be ascribed to the slightly poor quality of the crystal The Ortep plot, showing the asymmetric unit of the structure with 50% probability level and its numbering scheme, is illustrated in Figure 2. The asymmetric unit of Pt(ppy)K contains one atom of platinum, coordinated with a square planar geometry by a pyridine ring, a phenyl ring and two cyano groups (Fig. 1a). The asymmetric unit presents also a potassium atom coordinated by the two cyano groups and one molecule of water forming a hydrogen bridge (H2a) with N22 (bond distance 1.945 Å). The crystal packing, shown in Figure S5, is dominated by π-π staking among ppy ligands, with molecules arranged parallel to the (*ab*) plane. The intermolecular Pt-Pt distance is 3.395 Å. Further details about the crystal structure investigation may be obtained free of charge from The Cambridge Crystallographic Data Centre www.ccdc.cam.ac.uk/data_request/cif, by quoting the deposition number (CCDC)-2033576.
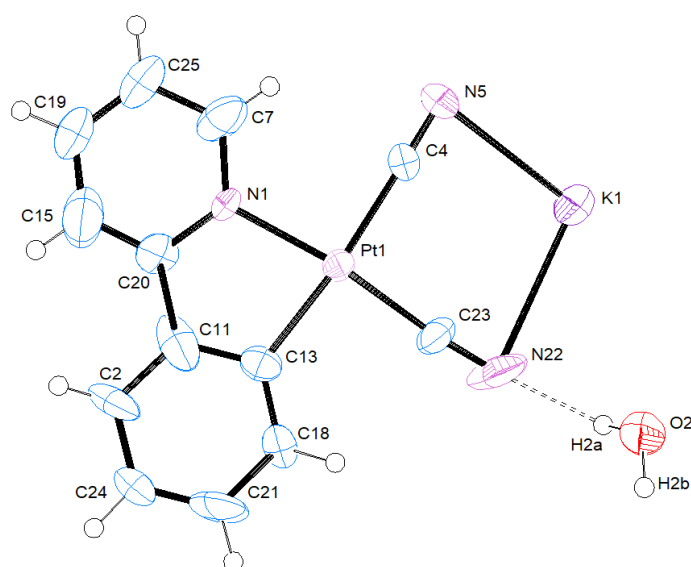

Figure 2. Ortep plot of the asymmetric unit of Pt(ppy)K.

3.1.2. *DFT calculations*

DFT calculations were conducted to help discriminating between two different structure solutions of Pt(ppy)K, namely one with the *Pca*2_1 symmetry and the other one with the *Pbca* symmetry. Using QUANTUM ESPRESSO [27], hence in a plane wave basis setup, the energy of both systems was minimized, first holding the cell geometry fixed and secondly relaxing also the cell stress. To this purpose, the PBE density functional with Grimme VdW correction was adopted. The integration grid in the reciprocal space had a resolution better than 0.11 Å^{-1} in all directions and was made approximately equal for both systems doubling the number of k points along the shortest direction of the *Pca*2_1 cell compared to the *Pbca* one. The computational parameters and the list of adopted core pseudopotentials are reported in Table S1. In both cases, the *Pbca* system proved to be more stable than the *Pca*2_1 one. In fact, after stress relief, *Pbca* was more stable than *Pca*2_1 by 0.27 eV/minimal formula, which is about 26 kJ/mol. The maximum deviation of the atomic positions in the computed structure compared to the structure derived from the diffraction data was 1.1 Å in the

symmetrical unit. The root-mean-square deviation of the non-hydrogen atoms in the *Pbca* symmetry between the experimental and DFT-optimized structures is 0.47 Å.

3.2. Static XRPD measurements

The static powder X-ray diffraction patterns (paragraph 2.4) of the vapochromic compounds listed in Table 1 are compared in Figure 3. The high similarity between powder profiles of Pt(bzq)K and Pd(bzq)K and of Pt(ppy)K and Pd(ppy)K indicates that the two compounds sharing the same ligand and counterion are isomorphic. As a consequence, it could be argued that a change of metal ion from Pt to Pd has a negligible effect on the crystal structure of the compounds. Instead a change of the ligand (from bzq to ppy) clearly affects the powder pattern, hence introduces modifications in the crystal structure. A similar, although greater, effect is observed for a change of the counterion (from K to Li), keeping constant the ligand and metal ion. In particular, a broadening of the diffraction peaks can be noted in Pt(bzq)Li compared with Pt(bzq)K, which points to a lower coherence length in the Li compound.
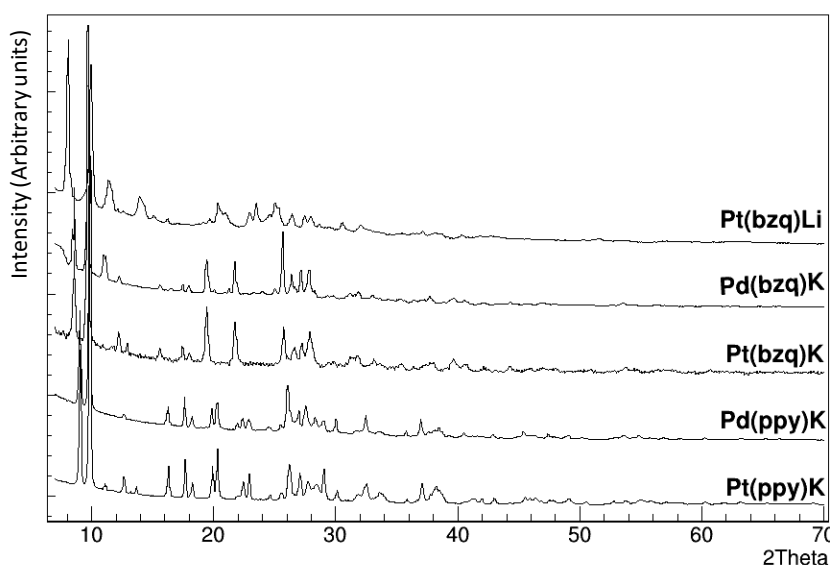

Figure 3 Comparison of X-ray powder diffraction patterns of the vapochromic compounds considered in this study. Data are shown up to 2ϑ=70°, but were collected up to 2ϑ=85°.

To quantify the above observations, we have assessed the crystallinity fraction and the average crystallite size. Results, shown in Figure 4, indicate that (i) the compounds with the ppy ligand have higher crystallinity than those with the bzq ligand; (ii) the Pt compounds exhibit a slightly higher crystallinity than Pd compounds with the same ligand; (iii) the crystallinity and crystallite size of the lithium compound is lower than those of the potassioum compounds. These evidences explains the successful re-crystallization of Pd(ppy)K, which is the most crystalline compounds, and the hygroscopic behaviour of Pt(bzq)Li, which has crystallites with smallest size, hence largest specific area.
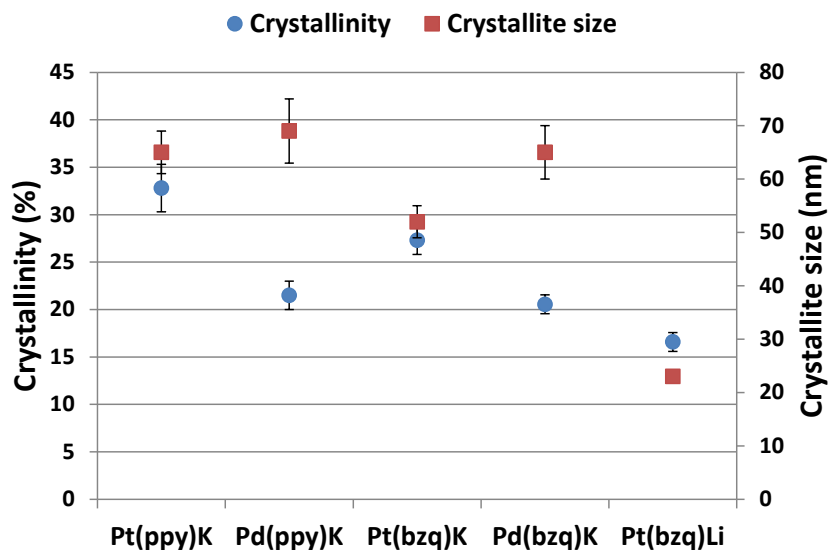
Figure 4 Crystallinity (circles, right axis) and average crystallite size (squares, left axis) estimated from the static X-ray powder diffraction profiles shown in Figure 5.

3.2.1 Pawley refinement

The cell parameters of Pt(ppy)K determined by single-crystal X-ray diffraction, collected at room temperature, were used in a profile-fitting procedure applied to its static powder X-ray diffraction pattern, also collected at room temperature (Figure 5a). The Pawley refinement converged to R_{wp} 8.91 and R_p 5.47 with the cell parameters reported in Table 3.
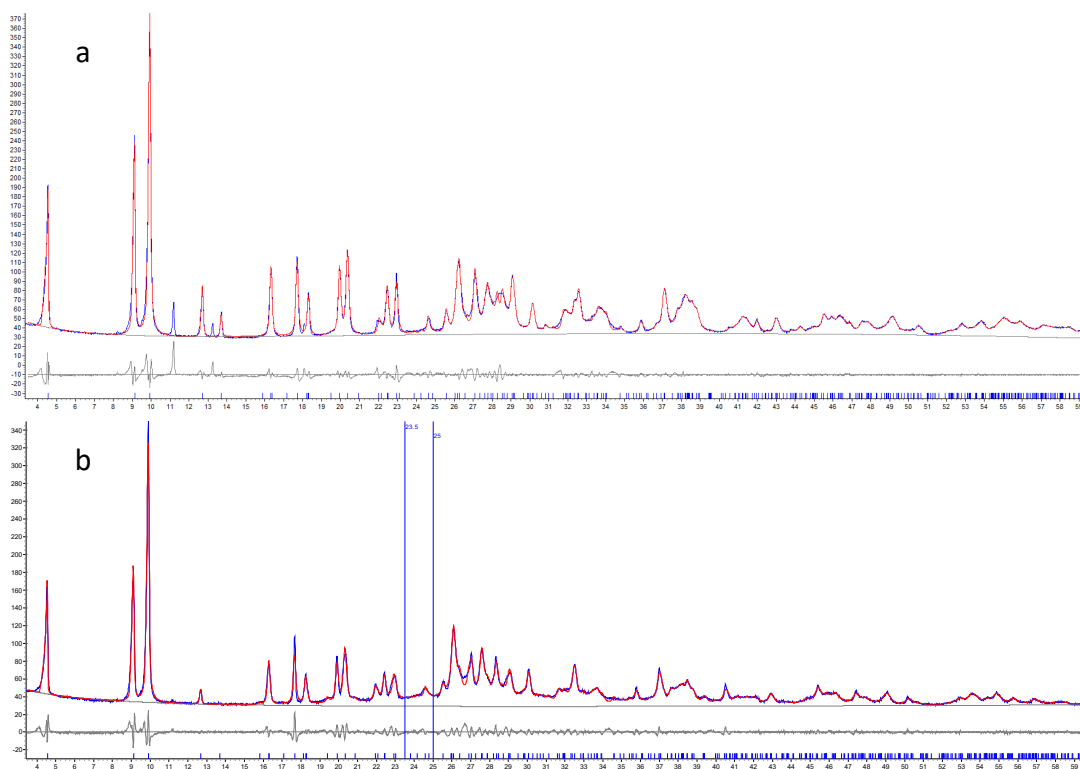
Figure 5. Pawley refinement of Pt(ppy)K (a) and Pd(ppy)K (b). The two peaks at 23.5° and 30.1° of 2θ are used to describe the capillary contribution. Data are shown up to 2θ=60°, but were collected up to 2θ=85°.

Few extra peaks at low 2θ angles are present in the pattern, which cannot be assigned to the cell. They were identified by qualitative analysis executed at the borderline condition of using only three experimental diffraction peaks (at 11.19, 13.25 and 18.09° 2θ) in the search-match process. The extra peaks can be attributed to the $K_2(Pt(CN)_4)(H_2O)_{0.713}$ compound [30], which is considered a secondary synthesis product. In fact, the positions of the highest diffraction peaks of $K_2(Pt(CN)_4)(H_2O)_{0.713}$ (from the database) match the positions of the observed spurious peaks.

The powder patterns of Pt(ppy)K and Pd(ppy)K suggest isomorphism (Figure 3), hence the orthrombic cell parameters of Pt(ppy)K were used for the Pawley refinement of the Pd(ppy)K pattern (Figure 5b), which converged to R_{wp} 9.60 and R_p 13.13 with the cell parameters listed in Table 3.

Table 3. Cell parameters and agreement factors determined by using the Pawley refinement of the Pt(ppy)K structural model obtained by single-crystal X-ray diffraction on high-resolution powder diffraction data.

	Pt(ppy)K	Pd(ppy)K
	Powder	Powder
a (Å)	10.0088(6)	10.0336(6)
b (Å)	6.8053(8)	6.8499(8)
c (Å)	38.719(1)	38.767(1)
Volume (Å³)	2637.3(3)	2664.5(3)
R_{wp}	8.91	9.60
R_p	5.47	13.13

3.2.2 Crystal structure determination for Pd(ppy)K

The crystal structure determination of Pd(ppy)K was based on the assumption that the compound is isostructural to Pt(ppy)K. Because of the availability of only microcrystalline powder for Pd(ppy)K, two approaches can be followed: 1) the crystal structure of Pt(ppy)K, in which the Pt atom is replaced by Pd, is refined by the Rietveld method; 2) the structure is solved by using a real-space method that starts from a structure model compatible with the expected geometry. We used the second approach which, starting from a structure model similar to the Pt(ppy)K one and introducing degrees of freedom that are varied, permits to confirm the assumption of isostructurality. The crystal structure of Pd(ppy)K was solved using *EXPO2014* by the real-space method (Simulated Annealing) in the same space group of Pt(ppy)K. The starting expected model of the Pd(ppy)K compound was assembled using two molecules: $Pd(ppy)(CN)_2$ and a biatomic fragment K-O. The geometry of $Pd(ppy)(CN)_2$ was optimized by using NWCHEM employing DFT with B3LYP functional [31]. The method is based on the minimization of the difference between observed and calculated intensities moving, within the unit cell, an expected molecular model by varying its position, orientation and conformation. For the structure solution, the angular range $3.0° < 2θ < 45.30°$ was used. A total of 9 parameters were optimized by *EXPO2014* during the minimization process: three coordinates to describe the position of the centre of mass, three angles describing the orientation and three torsion

angles to describe the conformation, for each molecular fragment. In a preliminary step the lattice constants of Pt(ppy)K were refined with the background and the peak shape parameters by the Le Bail strategy [32]. Finally, the global optimization algorithm was run 20 times in a default mode and the best solution with the lowest cost function $R_{wp} = 19.92$ was selected. Hydrogen atoms were not included in the optimization. Anti-bumping restraints (directive *bump* in *EXPO2014*) were used for avoiding unreliable conformations. The final large R_{wp} discrepancy factor value confirms the difficulty to recover the crystal structure also in the case of the Pd compound by using powder diffraction data. It is relevant that the structure model corresponding to the lowest cost function value is superimposable with the Pt(ppy)K model (Figure 6), so strenghtening the isomorphism hypothesis.
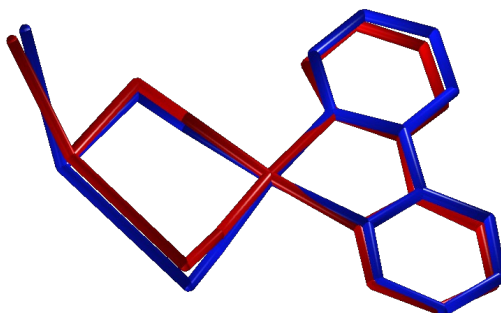

Figure 6. The best solution of Pd(ppy)K (blue) obtained from powder diffraction data by simulated annealing overlaid on the single-crystal structure of Pt(ppy)K (red), showing a good agreement. H atoms have been omitted for clarity.

3.3. Thermogravimetric analysis

A TGA was carried out to verify the actual loss of water from the material. The TGA curves of Pt(bzq)K (Figure S6) Pt(ppy)K (Figure S7) and Pd(ppy)K (Figure S8) show a weight loss of 4.1%, 3.9% and 5.2% respectively, which corresponds to one water molecule per molecule. Hence these compounds are monohydrate, as confirmed by the crystal structure of Pt(ppy)K. For Pt(bzq)K and Pt(ppy)K two well-separated stages of water loss occur just before and after the critical temperature for the vapochromic transition (see Figure 10. This is in agreement with what is reported in the literature [5] and indicates that the first water loss precedes the onset of the transition, and the second one continues just after it. A different behavior was observed for Pd(ppy), where the two stages of water loss are almost superposed and both occur before the critical temperature. This indicates that the type of metal ion strongly affects the mechanism of water loss. The weight loss observed for Pt(bzq)Li is 9.5% (Figure S9), which corresponds to 2.5 water molecules. Thus the exact formula of this compound is $[Li(H_2O)_{2.5}][Pt(bzq)(CN)_2]$. The higher degree of hydration and the higher hygroscopicity of this lithium salt compared to the potassium salts with the same ligand might be due to the lithium ion itself. A single, wide step of water loss can be identified in this case, which is centered at 50 °C and tails up to 140 °C. Thus both the total amount of water loss and its temperature dependence are highly influenced by the counterion.

3.4. In situ X-ray powder diffraction

Since these materials dehydrate upon heating, the structural changes that follow the dehydration transition were characterized by VTXRPD limited to compounds Pt(bzq)K, Pt(ppy)K and Pd(ppy)K. The occurrence of color and diffraction pattern variations as a function of temperature are schematized graphically in Figure S10.

Figure 7 reports the diffraction patterns collected for Pt(bzq)K: structural changes together with a change of color from dark red to yellow are observed between 70° C and 80° C then no further modifications in the diffraction patterns are detected, up to 135° C. Cooling from 135° C to room temperature, the color returns red when the temperature was around 50° C and the diffraction pattern collected is consistent with hydrate form.

For Pt(ppy)K (Figure 8) structural changes are observed between 80° C and 95° C and then no further modification in the diffraction pattern is observed up to 145° C. The change of color from dark violet to yellow starts together with the structural changes, however this change of color is complete only around 135° C. As for Pt(bzq)K, Pt(ppy)K returns dark violet upon cooling, at about 60° C and the diffraction pattern at room temperature corresponds to that of the hydrate form (Figure S11).

For Pd(ppy)K (Figure 9) structural changes together with change of color from yellow to white are observed between 75° C and 95° C. No further modification in the diffraction pattern was observed up to 105° C. Upon cooling, color and powder pattern of the hydrate form are restored (Figure S12).
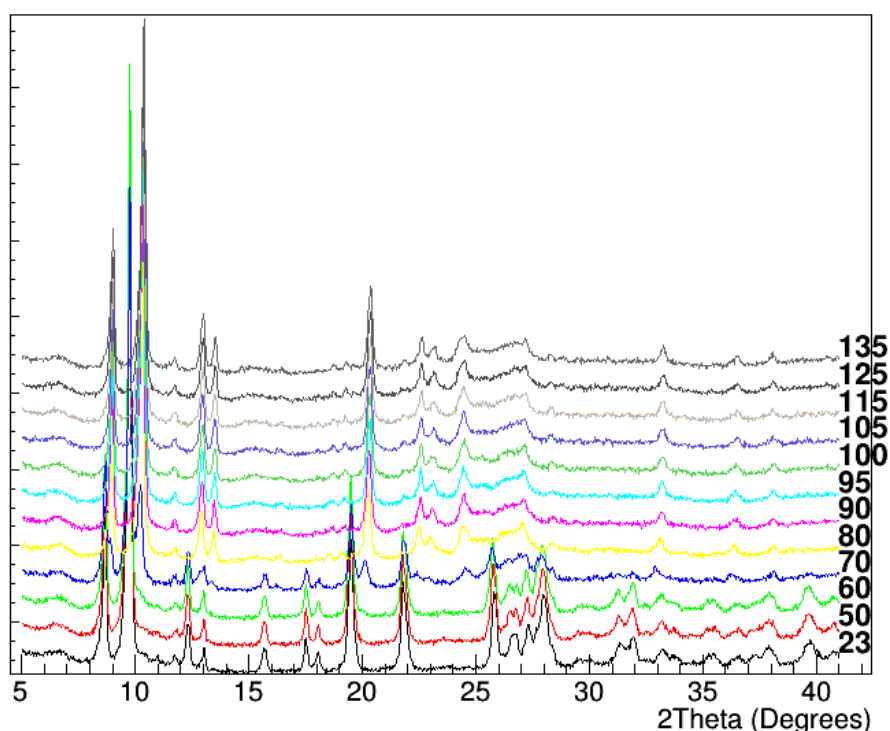

Figure 7. Varied-temperature X-ray diffraction analysis of compound Pt(bzq)K. Powder X-ray diffraction profiles measured in situ during heating.
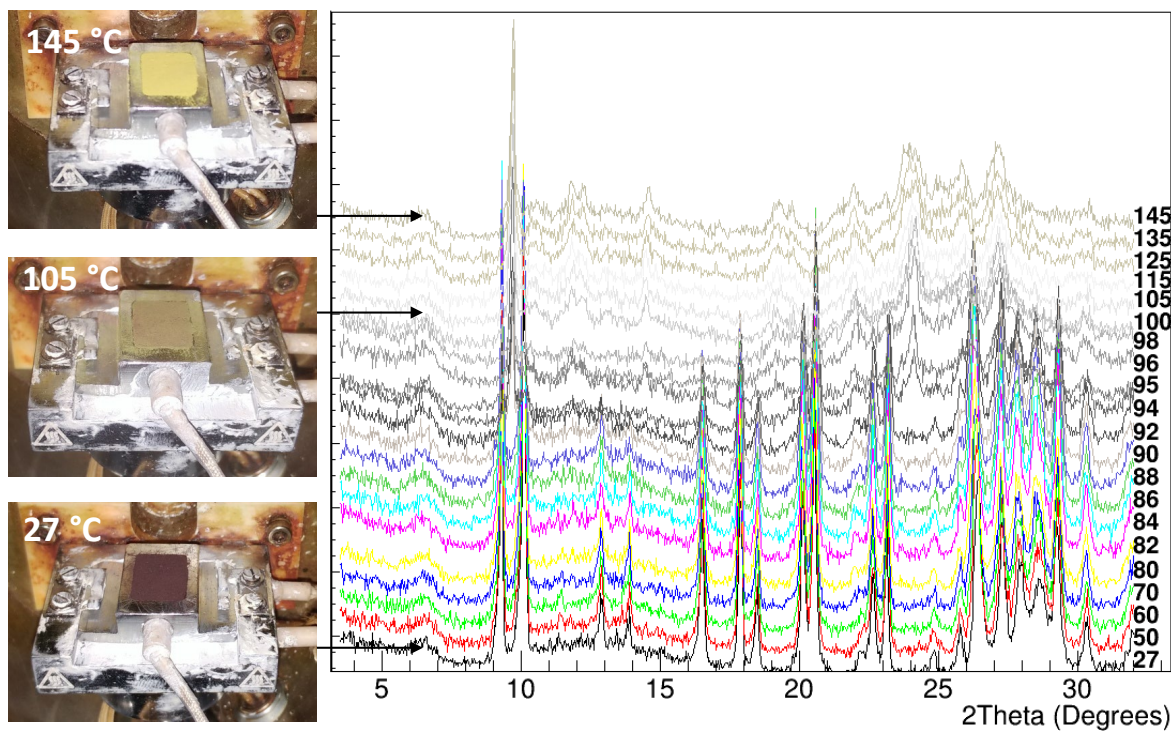
Figure 8. Varied-temperature X-ray diffraction analysis of compound Pt(ppy)K. Powder X-ray diffraction profiles measured in situ during heating (left) and color changes of the sample heated at 27° C, 105° C and 145° C (right).
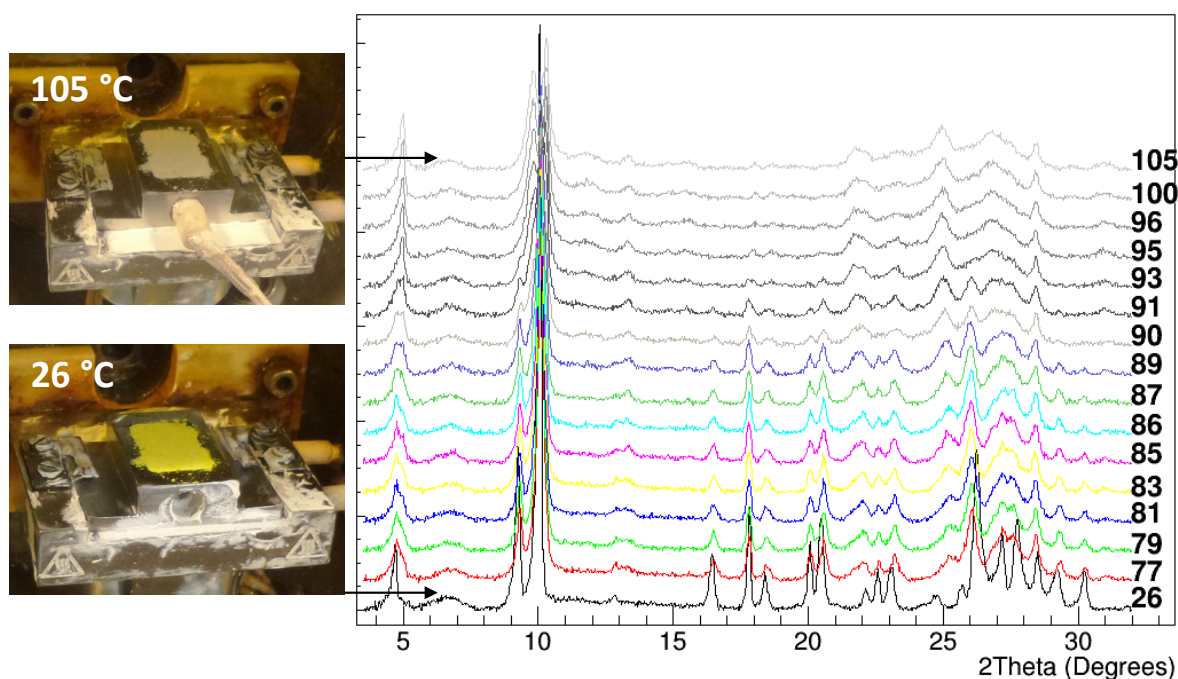

Figure 9. Varied-temperature X-ray diffraction analysis of compound Pd(ppy)K. Powder X-ray diffraction profiles measured in situ during heating (left) and color changes of the sample heated at 26° C and 105° C (right).

PCA applied to VTXRPD data matrices allows estimating the reaction coordinate, represented by the scores of the first principal component (PC1). They capture the trend of the global changes in the diffraction profiles as a function of temperature, and clearly represent an order parameter for the vapochromic transition (Figure 10). The reaction coordinate was used to perform a complete kinetic analysis (Figure S13). The most appropriate kinetic model to describe the vapochromic transitions of the three compounds was identified as the Avrami-Eroféev model, described by eq. (3). The kinetic parameters n, Ea and $log(A)$, together with the critical temperature, i.e. the temperature at which the reaction coordinate shows a flex, are reported in Table 4. It can be noted that compound Pt(bzq)K has a lower critical temperature than Pt(ppy)K and Pd(ppy)K, confirming the strong dependence of the vapochromic properties on the ligand already observed in [6]. Regarding the reaction order, it results that it is lower for Pt(ppy)K than for Pt(bzq)K, and it is lower for Pt(ppy)K than for Pd(ppy)K.
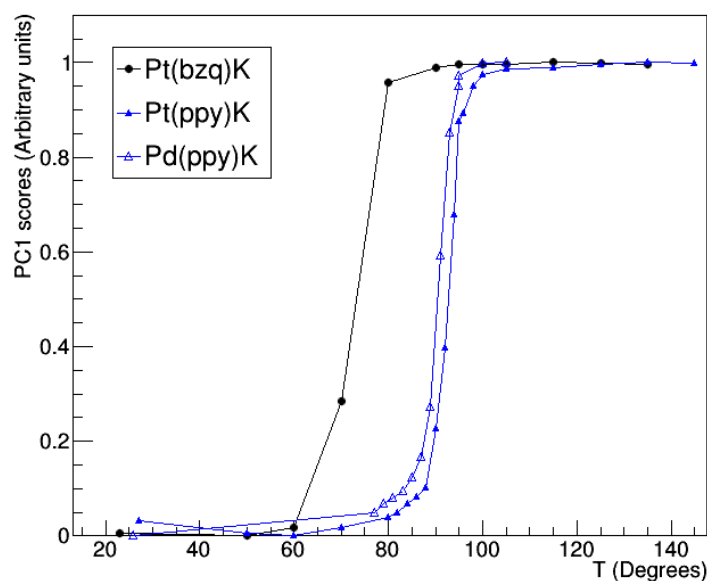

Figure 10. Reaction coordinate for the heating process of the vapochromic compounds, as determined by PCA applied to variable-temperature X-ray powder diffraction patterns. PC1 scores of the three compounds have been rescaled so that they span the values between 0 and 1, as they are calculated in arbitrary units.

Table 4. Results of kinetics analysis performed on VTXRPD measurements.

Compound	Critical temperature T (°C)	Critical temperature T (K)	Reaction order n	Activation Energy Ea (kJ/mol)	Frequency factor $Log(A)$ (s^{-1})
Pt(bzq)K	80	353	3.6±0.6	64±4	19±1
Pt(ppy)K	94	367	3.3±0.3	60±6	16±2
Pd(ppy)K	91	364	4.5±0.2	52±4	14±1

A characteristic feature of the VTXRPD profiles of the three compounds is an overall decrease of peak height with temperature. Quantitative estimation of the crystallinity of the samples, performed on each individual profile of the three compounds, are reported in Figure 11. It can be noted that the crystallinity fraction follows a trend very similar to that of the reaction coordinate (Figure 10). It is high at room temperature, has an abrupt decrease at a critical temperature, which for the three compounds corresponds to that reported in Table 4, and then remain constant to roughly the same value for each compound (20%). Pt(ppy)K has the highest crystallinity and the highest decrease upon the vapochromic transition.
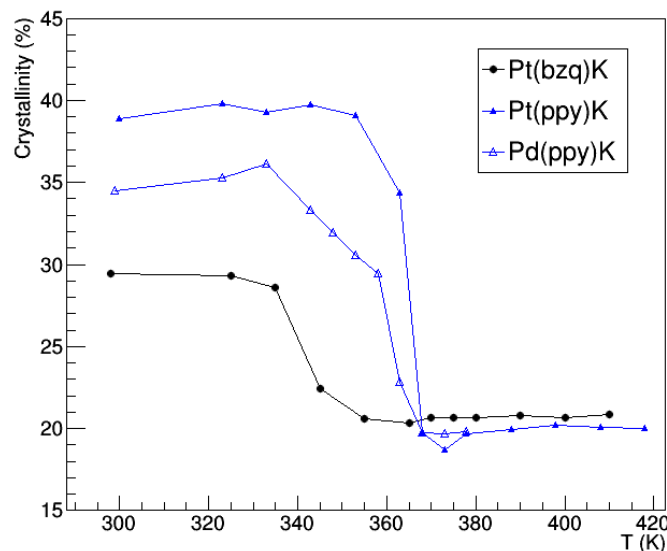

Figure 11. Crystallinity fraction determined from X-ray powder diffraction profiles as a function of the temperature on the sample.

3.5. In situ pair distribution function

PDF profiles obtained at different temperatures for samples with potassium as counterion are superimposed in Figure 12. As a common feature, abrupt changes in the PDF $G(r)$ profiles occur at interatomic distances larger than 8 Å, indicating the occurrence of substantial structural changes upon heating. Smaller variations among profiles are present at interatomic distances between 3.0 and 8.0 Å, and profiles remain almost constant for interatomic distances lower than 3.0 Å. Rademacher *et al.* [28] suggested that PDF profiles can be ideally divided into three regions: below 3 Å, where only intramolecular distances are present; between 3 and 8 Å, where intramolecular and intermolecular distances overlap, and beyond 8 Å, where only longer intermolecular distances are present. Not unexpectedly, this indicates that the molecule itself does not change its conformation upon heating, while crystal packing is strongly influenced by the vapochromic transition, so that the mutual position of different molecules in the crystal is varied. It can be also noticed that PDF curves tend to flatten in the intermolecular distances region as the temperature is increased, remaining almost constant for higher temperatures. This indicates a decrease of the long-range structural order, due to the deterioration of the crystal lattice, which has been also assessed by the crystallinity analysis of

VTXPRD data. Another feature arising from the analysis of Figure 12 is the similarity between PDF profiles at $r > 3$ Å of compounds, suggesting a similar local crystal packing.
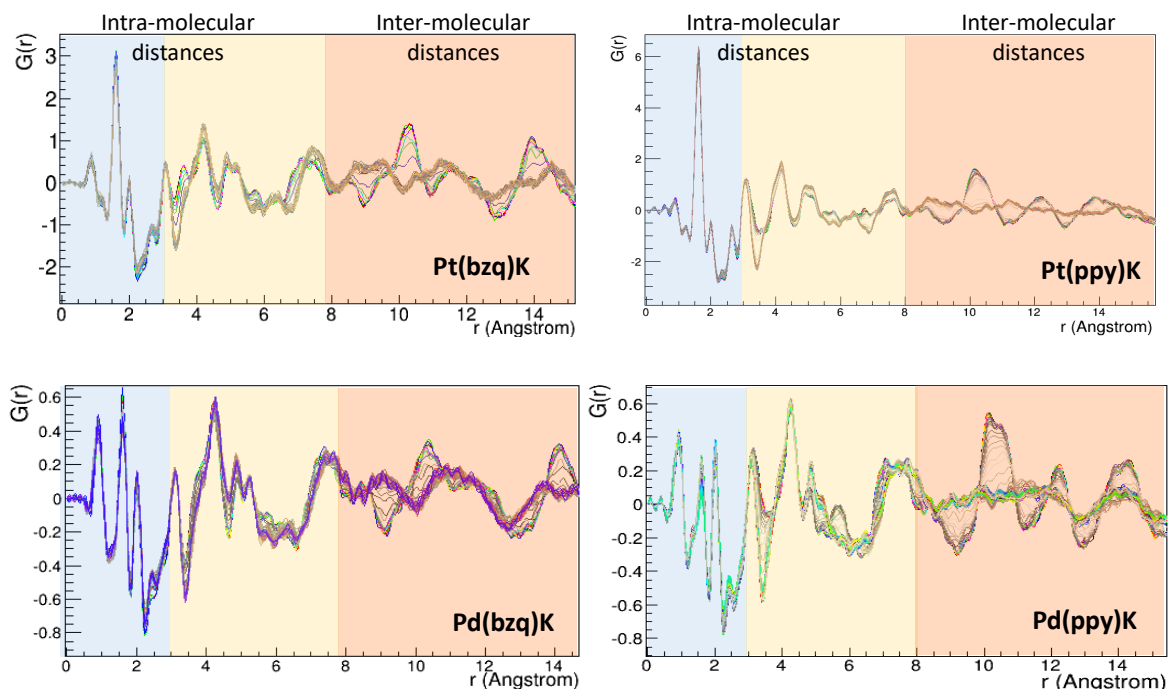

Figure 12. Overlap of *in situ* PDF profiles obtained while heating the vapochromic samples. Only the part with interatomic distance r <15 Å is shown. Three regions are highlighted, involving only intra-molecular distances (cyan), intra-molecular and inter-molecular distances (yellow) and only inter-molecular distances (brown).

Variations of PDF profiles as a function of temperature can be conveniently investigated by using a multivariate approach. For each compound, the PDF data matrix made of a set of 42 PDF profiles collected during heating (300 to 450 K) and cooling (450 to 350 K) steps constitutes the input for the principal component analysis (PCA). As a result, PCA scores and loadings are obtained for each compound as a function of the measurement number and of the interatomic distance, respectively. They are reported in Figures S15-S18, the interpretation of which should take into account a sign ambiguity in both PCA scores and loadings. The main features of the PDF profiles are captured by the first principal component (PC1), which explains more than 80% of the total data variance for all compounds. PC1 scores describe how structural variations evolve during measurements: for all compounds, they exhibit an abrupt change during the heating step and a constant trend while the temperature is ramped down. This implies a non-reversible vapochromic transition, contrary to evidences gathered from optical experiments [5], which could be due to an uneven air flow within the capillary preventing water molecules to get back to the region of the capillary hit by the X-ray beam during the cooling step. In fact, we noticed that only the part of the sample reached by the cryostream flux changed the color during the heating step, it remained unchanged during the cooling step, and returned to the original color long after the end of the experiment.

A PCA applied to different ranges of interatomic distances (Figure S19) indicates that the main contribution to the kinetic trend captured by PC1 comes from intra-molecular distances ($r >3$ Å). Nevertheless, a residual contribution arises from inter-molecular distances. In fact, the PC1 scores calculated by considering interatomic distances < 3 Å, while noisy, have the same main characteristics of those calculated from the

whole range. This implies that structural rearrangements related to the vapochromic transition mainly affect crystal packing, but have an effect also on the molecular units.

PC1 loadings represent the PDF signal associated to the kinetic behavior captured by the PC1 scores. For all compounds, they satisfy the basic expectations for typical PDF profiles listed by Chapman *et al.* [29], namely envelope with decreasing peak amplitude at high interatomic distances and limited presence of high-frequency components ($\nu \approx 2\pi/Q_{\max}$, which is the characteristic frequency in *r* space of ripple artefacts arising from the Fourier transform of scattering factors measured up to $Q_{\max}$). Thus, PC1 loadings most likely contain information from the part of the crystal structure that is involved in changes related to the vapochromic transition.

Interestingly, the sharp peaks of the PC1 loadings for all the compounds have the same positions, taking into consideration the above mentioned sign ambiguity (Figures S15-S18 and Figure 13), indicating similar structural changes triggered by temperature variations. The first peak occurs at an interatomic distance of about 3.2 Å, which is consistent with the typical Pt-Pt or Pd-Pd bond distance. Thus it is reasonable to assign such peaks to variations of metal-metal inter-molecular distances, which hence represent the main structural variations related to vapochromic transitions. Such evidence is in agreement with previous investigations about the optical properties of these compounds [5].

Higher-order principal components shown in Figures S15-S18 (PC2 and PC3) have scores that are strictly related to the PC1 scores. In fact, PC2 and PC3 scores do not follow the trend of temperature variations exerted on the sample during the experiment, instead they reproduce approximatively the first and second derivative of the PC1 scores, respectively. Interestingly, the same result is obtained for PCA applied to VTXPD data (Figure S14). Therefore structural changes captured by second-order principal components are not due to crystal lattice variations, rather they reflect second-order structural changes, different from those involving metal-metal distances within the crystal. For example, they could be related to changes in the orientation of molecules in the crystal.

PC2 and PC3 loadings in Figures S14-S17 reveal that compounds containing the bzq ligand are less affected by second-order structural rearrangements than those containing the ppy ligand. Whether a principal component hold significant signal or just noise depends on the features of their loadings. In particular, noise is dominant when loadings deviate from typical experimentally-derived PDF curves and hold high-frequency signals, close to $\nu \approx 2\pi/Q_{\max}$. With this criterion the following significative components can be recognized: PC2 for Pd(bzq)K; PC2 and PC3 for Pt(ppy)K and Pd(ppy)K. In fact, they have the typical envelope of experimentally derived PDF curves, with peak intensity decreasing with the interatomic distance, and lack of high-frequency components.

3.5.1. Comparative analysis based on PDF loadings

A way to compare vapochromic compounds based on their dynamical properties is to perform a comparative analysis taking PC1 loadings as representative of the behavior of each compound. In fact, PCA applied to *in situ* PDF data has shown that PC1 captures most of the data variance, and its loadings contain the structural information behind this variance, which is closely related to the vapochromic transition. The PC1 loadings are shown in Figure 13a. They have been used as input for a further PCA step (PCA'), which generated a PC2' vs PC1' score plot (Figure 13b) and PC1' and PC2' loadings (Figure 13c). From inspection of the score plot, it can be noted that the compounds are separated in PC1' (which accounts for 73.9% of the total data variance) according to the type of

ligand, while they are separated in PC2' (which accounts for 20.2% of the total data variance) according to the type of metal atom. This result confirms the relevance of the ligand in determining the behavior of the phase transition. The inspection of the PC1' and PC2' loadings suggests the short-range effect of variations of metal-metal distances during the vapochromic phase transition. In fact, PC2' loadings have a large contribution only for $r < 20$ Å. Conversely, the long-range effect of the ligand is dictated by PC1' loadings, whose amplitude increases for interatomic distances > 20 Å.
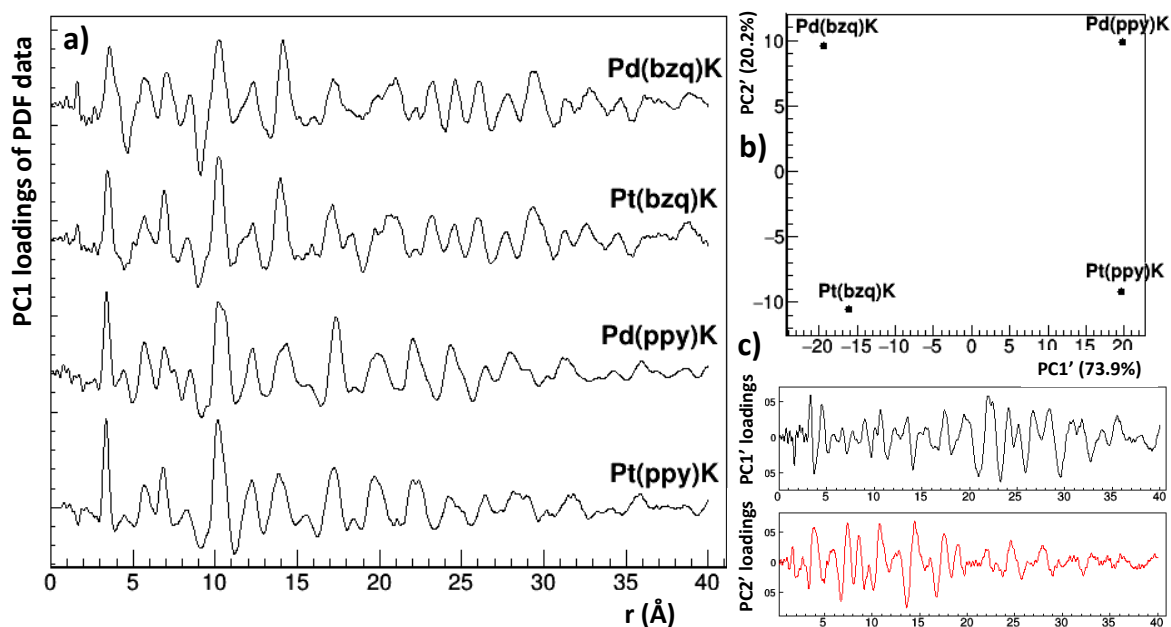

Figure 13. Comparison of vapochromic compounds based on PC1 loadings of their *in situ* PDF data. PC1 loadings (a) have been processed by a second step of PCA (P CA'), generating the PC2' *vs* PC1' score plot (b) and the PC1'and PC2' loadings (c).

3.5.2. Kinetic analysis of PDF data

The reaction coordinate for each compound during the heating process has been determined in the same way as done for the *in situ* X-ray powder diffraction data, *i.e.* by considering the PC1 scores versus the temperature values associated to the different measurements (Figure 14). They represent the kinetics of the main structural variations involved in the vapochromic transitions. From Figure 14 it can be seen that the critical temperature of the Pt(bzq)K and Pd(bzq)K compounds are lower than those of the Pt(ppy)K and Pd(ppy)K compounds, in agreement with what is reported in [6] and consistent with Figure 10. In addition, the slope of the reaction coordinate around the critical temperature (see inset of Figure 10) suggests that the transition of Pt(bzq)K and Pt(ppy)K compounds is sharper, *i.e.* the vapochromic transition occurs abruptly, than the transition of the corresponding compounds: Pd(bzq)K and Pd(ppy)K.
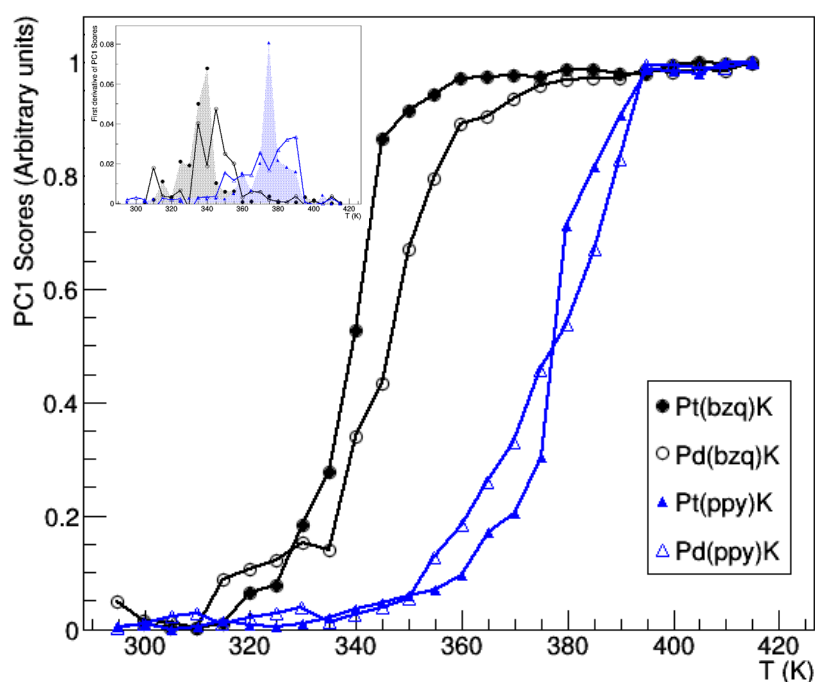
Figure 14. Reaction coordinate for the heating process of the vapochromic compounds, as determined by PCA applied to PDF profiles. PC1 scores of the three compounds have been rescaled so that they span the values between 0 and 1, as they are calculated in arbitrary units. Their first derivatives are shown in the inset.

A kinetic analysis of the reaction coordinate produces the results shown in Figure 15 and Table 5. Data are compatible with the kinetic model of Avrami-Eroféev for the four compounds, in agreement with what was found from VTXRPD data. Considering the same metal ion, the reaction order (n) is higher for the benzoquinolinato (bzq) than for the phenylpyridinato (ppy); considering the same ligand it is higher for Pd than for Pt. This reflects the above-mentioned trend of the reaction coordinate (Figure 14), as the reaction order is related to the slope of the transition curve at the critical temperature (lower-order transitions are steeper). Therefore, results from the kinetic analysis are consistent with the steeper rise of the reaction coordinate with temperature of the compunds with the ppy ligand with respect to those with the bzq ligand, and for compounds with the Pt metal ion with respect to those with the Pd one. The dependence of the reaction order on the ligand and on the metal ion agrees with that obtained from VTXPRD data, however the absolute values of the kinetic parameters are not compatible for the two experiments. Such discrepancies could be due to the different sample holders used (capillary versus flat holder) and to the different rate of temperature changes.
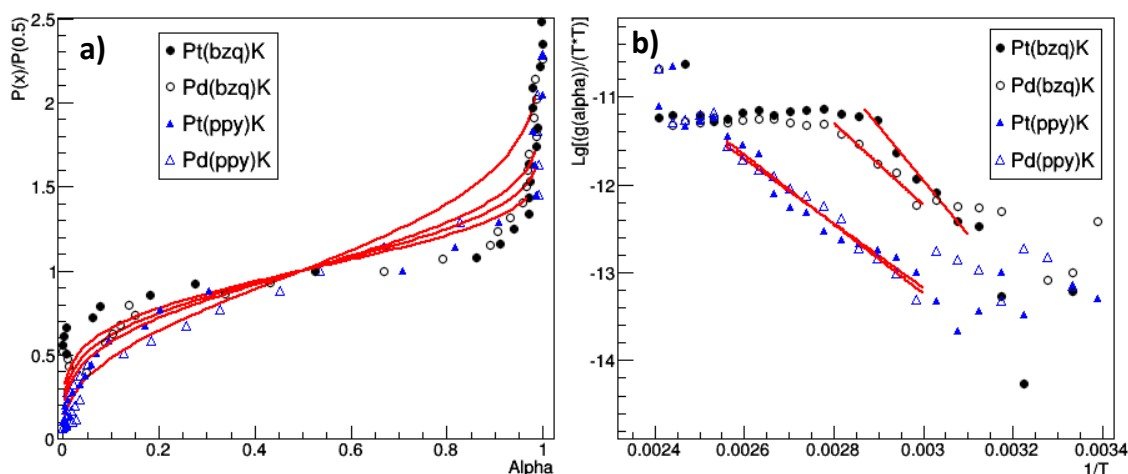
Figure 15. Results of the kinetic analysis performed on PDF data.

Table 5. Results of kinetics analysis performed on PDF measurements.

Compound	Critical temperature *T* (K)	Reaction order *n*	Activation Energy *Ea* (kJ/mol)	Frequency factor *Log(A)* (s⁻¹)
Pt(bzq)K	340	3.4±0.3	30±3	3±1
Pd(bzq)K	350	3.7±0.2	18±3	-2±1
Pt(ppy)K	380	3.2±0.1	23±2	-1.1±0.7
Pd(ppy)K	380	3.6±0.2	21±1	-1.7±0.3

3.5.3. Structural investigation of the vapochromic transition by PDF fitting

The crystal structure solution obtained for Pt(ppy)K was used to fit the PDF data of the same compound, and of the isomorphic compound Pd(ppy)K. By properly modifying the ligand structure, it was also used to fit Pt(bzq)K and Pd(bzq)K, assuming the same crystal symmetry and initial crystal cell. For all compounds, a good agreement between the fitted model and PDF data was reached at all temperatures spanned by the *in situ* experiments (Figures S20 and S21). As a result, for each vapochromic compound, we obtained an approximated solution for each step of the vapochromic transition, under the hypothesis that the crystal symmetry does not change in the process. The structural changes involved in the phase transition can be then inspected considering the structural parameters variations with temperature. The trend of the metal-metal distance and of the cell parameters, shown in Figure 16, reveals the following common features for all compounds. The metal-metal distance is about 3.4 Å at room temperature and increases up to about 3.9 Å after the phase transition. The molecular distancing is due to an increase of the *b* axis upon vapochromic transition, however this is not accompanied by a crystal cell expansion as it could be expected, but on the contrary by its contraction. In fact, the *a* cell parameter for Pt(ppy)K and Pd(ppy)K and the *c* cell parameter for Pt(bzq)K and Pd(bzq)K decrease upon the transition, in both cases determining a

comparable overall decrease of the crystal cell volume. The volume contraction is larger than what expected from the loss of one or two water molecules, thus necessarily involves rearrangements of molecular packing. Structural changes involving the metal ion and those involving crystal packing occur at the same critical temperature, which notably are systematically higher of about 10 K than those obtained from PC1 scores. This could be interpreted by considering that variations of cell parameters and metal-metal distances are preceded by second-order variations (local distortions, increased thermal motion) that are hidden when considering only the coordinates of the average structure.
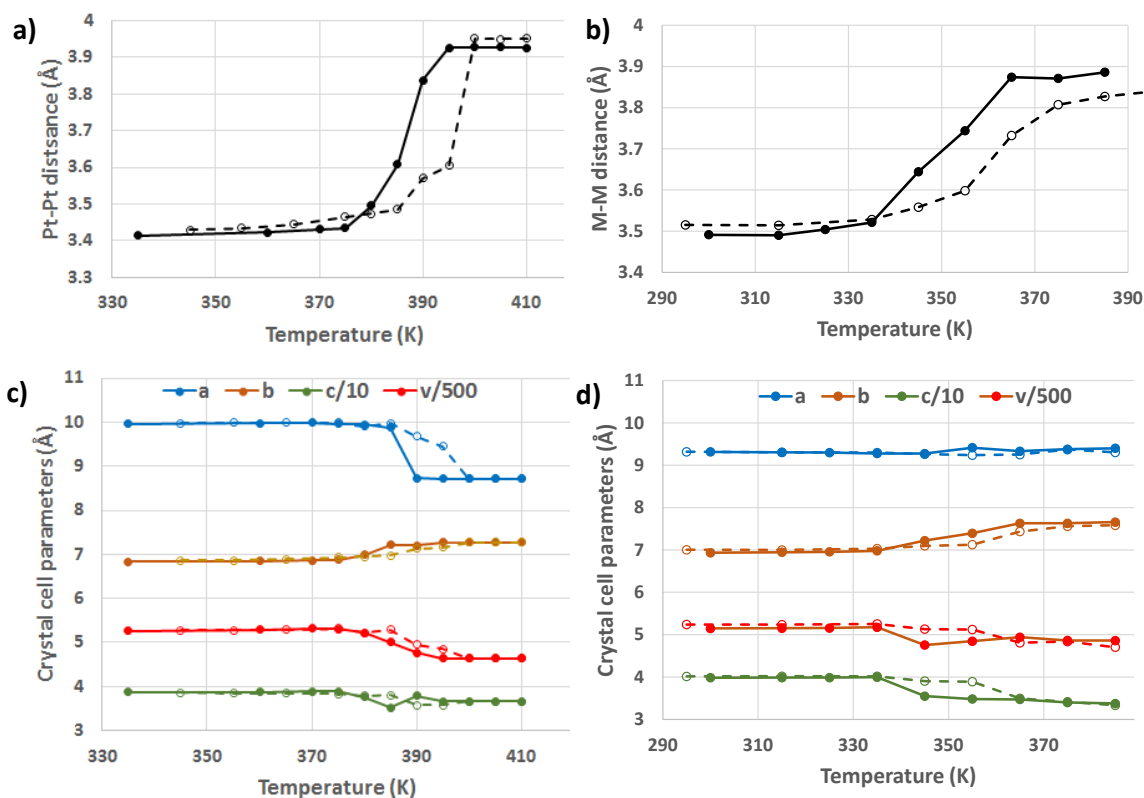

Figure 16. Structural parameters derived from the refinement of *in situ* PDF data. Metal-metal distance (a, b) and cell parameters (c,d) as a function of temperature for compounds Pt(ppy)K (full circles, full lines) and Pd(ppy) (open circles, dashed lines) (a,c), and Pt(bzq)K (full circles, full lines) and Pd(bzq)K (open cicles, dashed lines) (b,d).

Further insight into structural changes related to vapochromic transition can be gained comparing the refined crystal structures before and after the vapochromic phase transition (Figure 17). The most relevant feature is the variation of metal ion positions of symmetry-equivalent molecules, which at high temperature are not aligned along the *b* axis. This explains the increase in metal-metal distances reported in Figure 16. Viewing crystal packing along the *ac* plane (Figure 17) it can be noted a reduction of the spacing among molecules, in agreement with the decrease of the crystal cell volume reported in Figure 16. Another interesting feature can be revealed by viewing crystal packing along the *ab* plane: at room temperature molecules are packed so that they are aligned along the *b* axis in an alternated sequence, thus forming a zigzag curve; after phase transition molecules are perfectly aligned along the *b* axis, despite the shift of their metal centers. It can be concluded that the ligand

alignment compensates the metal misalignment, making the molecular arrangement compatible with a reduced crystal cell volume.
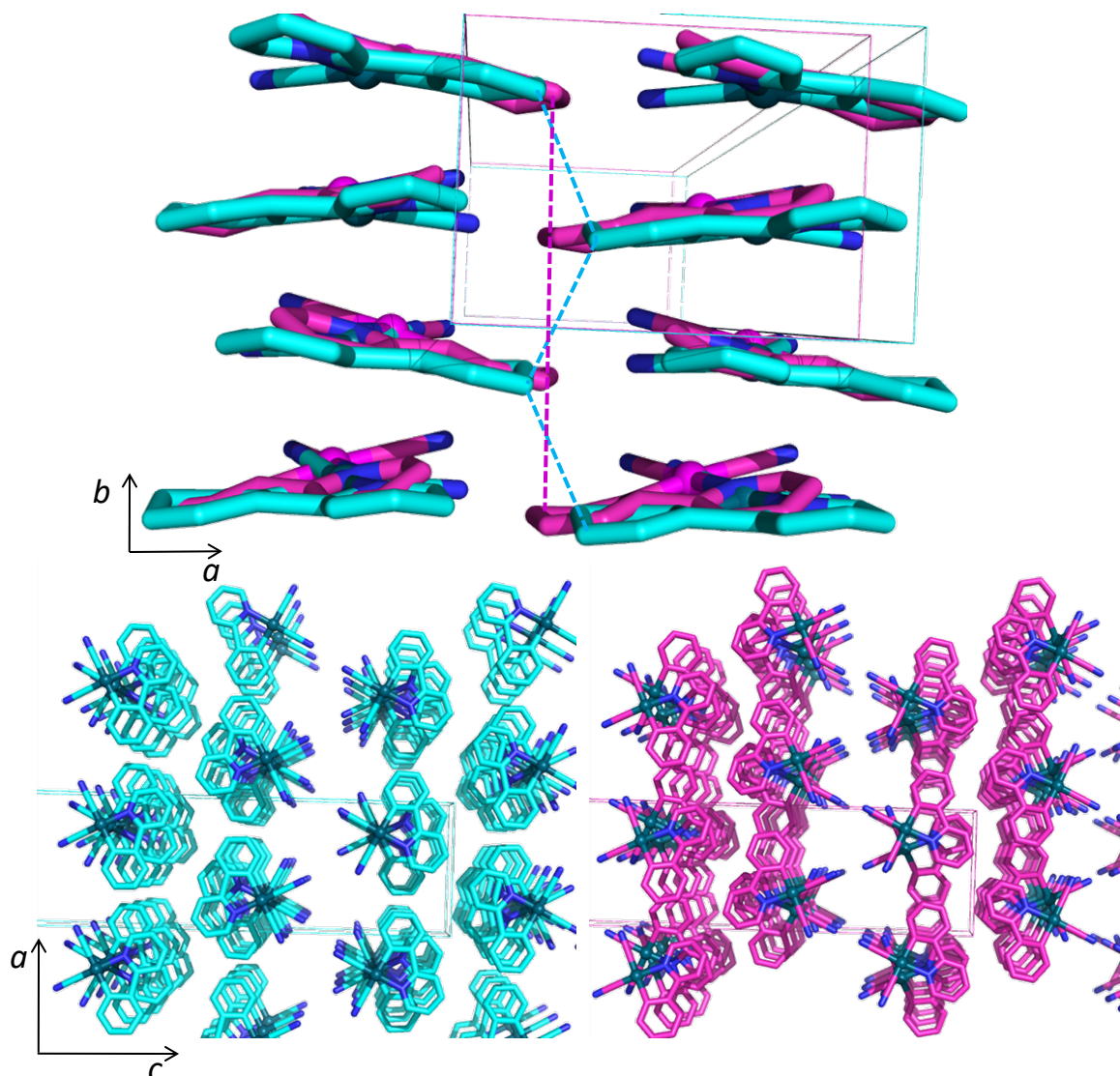

Figure 17. Structural comparison of crystal structures of Pt(ppy) refined against 300 K (cyan) and 450 K (pink) PDF data. View of the *ab* plane (top) and of the *ac* plane (bottom).

3.6. X-ray absorption spectroscopy

The PDF fitting analysis has been validated by using XAS data collected for Pt(bzq)K at room and high temperature. Structural information about the coordination of the platinum ion, and in particular the Pt-Pt distance, was checked against the EXAFS region of XAS data. The structural models of Pt(bzq)K obtained by the PDF data analysis at room and high temperature were used as the starting model for XAS data analysis. In the fitting procedure, the benzoquinolate and the two cyanide ions were considered as three separate rigid bodies. Scattering paths related both to single and multiple scattering events with amplitude reduction factor higher than 30% and scattering

distance lower than 4.1 Å were considered. In the first step of the fitting procedure, distances and Debye–Waller factors of the atoms in the first shell of platinum ion were used as free parameters. In this step, also the global parameters of amplitude reduction factor and of the shift of the absorption edge have been left free. Then, the value of such parameters was set to the best value obtained by the fitting. In the second step, the Debye–Waller factors of the remaining atoms belonging to the complex were left free, while their distances were calculated based on molecule geometry and the scattering path distances obtained in the first step. This procedure allowed keeping the number of independent points of the data higher than the number of variables used in the fitting. Finally, by keeping constant the value of the parameters related to atoms belonging to the complex, the inter-molecular Pt-Pt distance (highlighted by arrows in Figure S22) was used as a free parameter in the fitting. Such a procedure (results shown in Figure 18) provided a Pt-Pt distance of 3.3±0.5 Å and 3.9±0.1 Å for the complex at room and high temperature, respectively, in full agreement with the values obtained from the PDF fitting analysis. The values of the Pt Debye–Waller factor are 0.002 Å^2 and 0.005 Å^2, respectively at room and high temperature (this parameter has been fixed, thus error is not available).
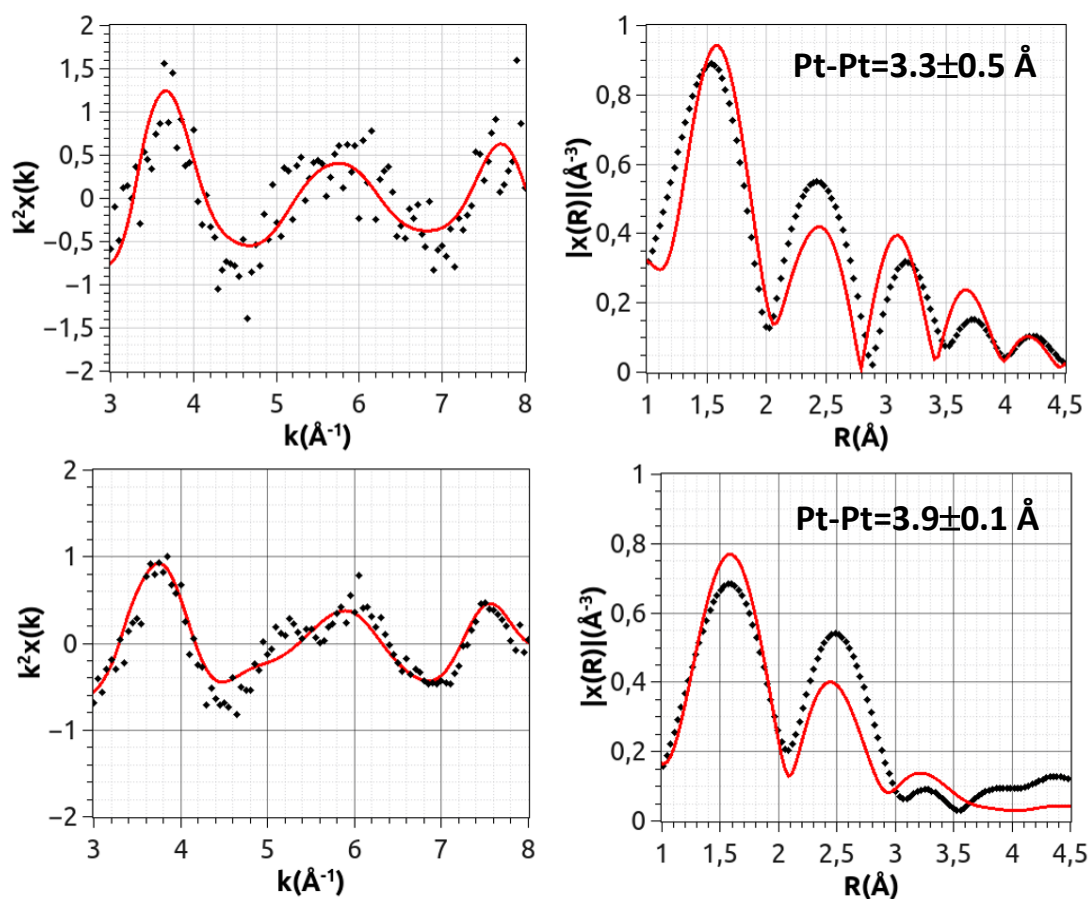

Figure 18. X-ray absorption spectroscopy analysis applied to Pt(bzq)K at low (top row) and high (bottom row) temperature: normalized XAS signal (left) and its radial distribution (right). The best-fit values of the Pt-Pt distance are shown.

4. Conclusion

The structural characterization of Pt- and Pd-based compounds considered in this study turned out to be a challenge not only for the large structural changes involved in the vapochromic transition, but also because of the non-homogeneity of the structural variations and the presence of impurities in the samples. These effects hindered a precise indexing of XRPD profiles collected in static and dynamical conditions. The challenge has been tackled by putting together several experimental techniques, by highlighting local features thanks to PDF measurements, and by processing experimental data with powerful computational tools.

The hydrated and anhydrous forms of the compounds have been compared by NMR and UV-vis spectroscopy; the temperature-dependent behavior of the vapochromic compounds has been studied by *in situ* X-ray diffraction, complemented by thermogravimetric analysis and visual inspection of color changes. Such combined analysis allowed to relate color changes, structural variations and water losses to temperature.

Characteristic curves describing the kinetics of the transition have been extracted by using a multivariate analysis approach applied to *in situ* X-ray diffraction measurements, and converging evidences were obtained by analyzing lab XRPD and synchrotron PDF measurements. The Avrami-Eroféev model is identified as the kinetic model best describing the vapochromic transition of all analyzed compounds. A strong dependence on the ligand forming the vapochromic compound was found, since the bzq ligand triggers a higher-order (smoother) transition occurring at a lower temperature than the ppy ligand, which triggers a lower-order (steeper) transition occurring at a 38 K higher temperature. Moreover, the kinetics of the transition is also influenced by the metal ion, with Pt compounds undergoing a lower-order transition than Pd compounds.

Even in the absence of detailed structural information, PCA results suggests that metal-metal contacts play a major role in determining the structural changes related to the vapochromic behavior. For Pt(ppy)K and Pd(ppy)K compounds, such changes are accompanied by structural distortions of the ligand structure, evidenced by more significant contributions from higher-order principal components.

Crystallinity measurements indicate that for all compounds the vapochromic transition is accompanied by an order-disorder transition having the same critical temperature.

Recrystallization experiments lead to the formation of crystals suitable for structural analysis only for compound Pt(ppy)K, for which the room-temperature crystal structure has been determined. This partial structural knowledge disclosed the possibility to investigate other compounds as a function of the temperature. In fact, bringing the PDF analysis to the extreme of its potential, this structural model was refined against each of the PDF profiles describing the compounds as a function of temperature. This has been achieved despite the increasing disorder in the crystal lattice, thanks to the local character of PDF measurements, and has been validated by XAS measurements. In this way, we got an insight into the structural rearrangements, comprising crystal cell distortions and changes of intermolecular distances accompanying the vapochromic transition. It was then possible to associate the different kinetics shown by the reaction coordinate of bzq and ppy compounds to a different mechanism of cell contraction during the vapochromic transition: it is mainly due to a reduction of the *c* cell paramteter for Pt(bzq)K and Pd(bzq)K and of the *a* cell parameter for Pt(ppy)K and Pd(ppy)K. On the other hand, the type of metal ion influenced the rate of changes in metal-metal distances, with Pt-Pt distances changing more rapidly than Pd-Pd distances.

The structural information obtained provides further insight into strategies to achieve engineered vapochromic complexes, which selectively and rapidly respond to specific vapors in small quantities.

Supporting Information. UV-visible and NMR spectra of Pd(bzq)K, Pd(ppy)K and Pt(bzq)Li compounds in their hydrated and anhydrous forms. Unit cell of the crystal structure solution of Pt(ppy)K. Computational parameters used in DFT calculations. Thermogravimetric analysis curves of Pt(ppy)K, Pd(ppy)K and Pt(bzq)Li. Schematic representation of structural and color variations of Pt(bzq)K, Pt(ppy)K and Pd(ppy)K. Comparison of X-ray powder diffraction profiles of the hydrated and anhydrous forms of Pt(ppy)K and of Pd(ppy)K before and after exposure to water vapors. Results of PCA and kinetic analysis performed on *in situ* X-ray powder diffraction data for Pt(bzq)K, Pt(ppy)K and Pd(ppy)K and on *in situ* PDF data for Pt(bzq)K, Pd(bzq)K, Pt(ppy)K and Pd(ppy)K. Results of PDF refinement of structural model at room temperature and at 450 K for Pt(bzq)K, Pd(bzq)K, Pt(ppy)K and Pd(ppy)K. Details about the X-ray absorption spectroscopy experiment and data analysis.

Corresponding Author

* Rocco Caliandro: rocco.caliandro@ic.cnr.it

Author Contributions

A.A. and R.C. conceived and supervised the project; S.F. and V.S. synthetized the vapochromic compounds and performed crystallization experiments; Ch.C. and A.F. performed re-crystallization experiments; F.M. and L.M. performed single-crystal X-ray diffraction (XRD) experiments; F.M. and A.F. performed XRD structure refinement; Ch.C. performed thermogravimetry experiments; R.R., C.C. and A.A. performed powder X-ray diffraction (PXRD) experiments; R.R. performed PXRD crystal structure solution; E.D. and R.C. performed PDF experiments; B.D.B. and R.C. performed multivariate and kinetic analysis; F.C. performed DFT calculations; R.C. refined crystal structures against PDF data; L.M., A.A. and R.C wrote the manuscript; all authors commented on the manuscript.

References

1.   Buss, C.E.; Anderson, C.E.; Pomije, M.K.; Lutz, C.M.; Britton, D.; Mann, K.R. Structural investigations of vapochromic behavior. X-ray single-crystal and powder diffraction studies of [Pt(CN-iso-C3H7)4][M(CN)4] for M = Pt or Pd. J. Am. Chem. Soc. 1998, 120, 7783–7790.

2.   Daws, C.A.; Exstrom, C.L.; Sowa, J.R.; Mann, K.R. Vapochromic compounds as environmental sensors. 2. Synthesis and near infrared and infrared spectroscopy studies of [Pt(arylisonitrile)4]x[Pt(CN)4] upon exposure to volatile organic compounds vapors Chem. Mater. 1997, 91, 363–368.

3.   Kobayashi, A.; Kato, M. Vapochromic Platinum(II) Complexes: Crystal Engineering toward Intelligent Sensing Devices Eur. J. Inorg. Chem. 2014, 27, 4469–4483.

4.   Wenger, O.S. Vapochromism in Organometallic and Coordination Complexes: Chemical Sensors for Volatile Organic Compounds 2013, 113, 3686–3733.

5.   Forniés, J.; Fuertes, S.; López, J.A.; Martín, A.; Sicilia, V. New water soluble and luminescent platinum(II) compounds, vapochromic behavior of [K(H2O)][Pt(bzq)(CN)2], new examples of the influence of the counterion on the photophysical properties of d8 square-planar complexes Inorg.Chem. 2008, 47, 7166–7176.

6.   Caliandro, R.; Belviso, B.D.; Cuocci, C.; Fuertes, S.; Sicilia, S.; Hanson, J.C.; Tutuncu, G.; Doorhyee, E.; Altomare, A. Dynamic characterization of structural changes in vapochromic compounds by pair distribution function Powder Diffraction 2017, 32, S118–S122.

7.   Altomare, A.; Caliandro, R.; Cuocci, C.; Giacovazzo, C.; Moliterni, A.G.G.; Rizzi, R.; Platteau, C.J. Direct methods and simulated annealing: a hybrid approach for powder diffraction data. J. Appl. Cryst. 2008, 41, 56–61.

8.   Á. Díez, J. Forniés, S. Fuertes, E. Lalinde, C. Larraz, J. A. López, A. Martín, M. T. Moreno, V. Sicilia Synthesis and Luminescence of Cyclometalated Compounds with Nitrile and Isocyanide Ligands Organometallics 2009, 28, 6, 1705–1718.

9.   Ravel, B., Newville, M., 2005. ATHENA, ARTEMIS, HEPHAESTUS: data analysis for X-ray absorption spectroscopy using IFEFFIT. Journal of Synchrotron Radiation 12, 537–541.

10.   Altomare, A., Corriero, N., Cuocci, C., Falcicchio, A., Moliterni, A. and Rizzi, R. QUALX2.0: a qualitative phase analysis software using the freely available database POW_COD J. Appl. Cryst. 2015 48, 598-603.

11.   Altomare, A.; Cuocci, C.; Giacovazzo, C.; Moliterni, A.; Rizzi, R.; Corriero, N; Falcicchio, A. EXPO2013: a kit of tools for phasing crystal structures from powder data. J. Appl. Cryst. 2013, 46, 1231-1235.

12.   Rigaku Oxford Diffraction, (2020), CrysAlisPro Software system, version 1.171.40.69a, Rigaku Corporation, Oxford, UK.

13.   Burla, M.C.; Caliandro, R.; Carrozzini, B.; Cascarano, G. L.; Cuocci, C.; Giacovazzo, C.; Mallamo, A.; Mazzone A.; Polidori G. Crystal structure determination and refinement via SIR2014, J. Appl. Cryst. 2015, 48, 306–309.

14.   Sheldrick, G.M. Crystal structure refinement with SHELXL. Acta Crystallogr. Sect. C Struct. Chem. 2015, 71, 3–8.

15. Macrae, C.; Edgington, P.R.; McCabe, P.E.; Pidcock, E.; Shields, G.; Taylor, R.; Towler, M.; Van De Streek, J. Mercury: Visualization and analysis of crystal structures. J. Appl. Crystallogr. 2006, 39, 453–457.

16. Farrugia, L. J. WinGX and ORTEP for Windows: an update, J. Appl. Cryst. 2012, 45, 849–854.

17. Hammersley, A.P.; Svensson, S.O.; Hanfland, M.; Hauserman, D. Two-dimensional detector software: From real detector to idealised image or two-theta scan High Press. Res. 1996, 14, 235–248.

18. Juhás, P.; Davis, T.; Farrow, C.L.; Billinge, S.J.L. PDFgetX3: a rapid and highly automatable program for processing powder diffraction data into total scattering pair distribution functions J. Appl. Cryst. 2013, 46, 560–566.

19. Juhás, P.; Farrow, C.L.; Yang, X.; Knox K.R.; Billinge S.J.L. Complex modeling: a strategy and software program for combining multiple information sources to solve ill posed structure and nanostructure inverse problems Acta Cryst. A 2015 71, 562–568.

20. Caliandro, R.; Belviso B.D. RootProf: software for multivariate analysis of unidimensional profiles J. Appl. Cryst. 2014, 47, 1087–1096.

21. Wold, S.; Esbensen, K.; Geladi, P. Principal Component Analysis Chemom. Intell. Lab. Syst. 1987, 2, 37–52.

22. Ryan, C.G.; Clayton, E.; Griffin, W.L.; Sie, S.H.; and Cousens, D.R SNIP, a statistics-sensitive background treatment for the quantitative analysis of PIXE spectra in geoscience applications Nucl. Instrum. Methods Phys. Res. Sect. B, 1988, 34, 396–402.

23. Scherrer, P.; Bestimmung der Größe und der inneren Struktur von Kolloidteilchen mittels Röntgenstrahlen. Göttinger Nachrichten Math. Phys. 1918, 2, 98–100.

24. Guccione, P.; Palin, L.; Belviso, B.D.; Milanesio, M.; Caliandro, R. Principal component analysis for automatic extraction of solid-state kinetics from combined in situ experiments Phys. Chem. Chem. Phys. 2018, 20, 19560–19571.

25. Coats A.W.; Redfern J.P. Kinetic Parameters from Thermogravimetric Data Nature, 1964, 201, 68-69.

26. Al-Khamis, K.M.; Al-Othman, Z.A.; Mahfouz, R.M. Kinetic Studies of the Non-Isothermal Decomposition of Unirradiated and γ-Irradiated Gallium Acetylacetonate Progress in Reaction Kinetics and Mechanism, 2010, 35, 131–151.

27. Giannozzi, P.; Baroni, S.; Bonini, N.; Calandra, M.; Car, R.; Cavazzoni, C.; Ceresoli, D.; Chiarotti, G. L.; Cococcioni, M.; Dabo, I.; Dal Corso, A.; Fabris, S.; Fratesi, G.; de Gironcoli, S.; Gebauer, R.; Gerstmann, U.; Gougoussis, C.; Kokalj, A.; Lazzeri, M.; Martin-Samos, L.; Marzari, N.; Mauri, F.; Mazzarello, R.; Paolini, S.; Pasquarello, A.; Paulatto, L.; Sbraccia, C.; Scandolo, S.; Sclauzero, G.; Seitsonen, A.P.; Smogunov, A.; Umari, P.; Wentzcovitch, R.M. QUANTUM ESPRESSO: a modular and open-source software project for quantum simulations of materials J. Phys.: Condens. Matter 2009, 21, 395502.

28. Rademacher, N.; Daemen, L.L.; Chronisterc E.L.; Proffen, T. Pair distribution function analysis of molecular compounds: significance and modeling approach discussed using the example of p-terphenyl J. Appl. Cryst. 2012, 45, 482–488.

29.   Chapman, K.W.; Lapidus, S.H.; Chupas, P.J. Applications of principal component analysis to pair distribution function data J. Appl. Cryst. 2015, 48, 1619–1626.

30.   Muehle, C. Nuss, J. Dinnebier, R.E. Jansen, M., Ueber Kaliumtetracyanoplatinat(II), Kaliumtetracyanopalladat(II) und deren Monohydrate Zeitschrift fuer Anorganische und Allgemeine Chemie, 630, 2004, 630, 1462–1468.

31.   Valiev, M., Bylaska, E. J., Govind, N., Kowalski, K., Straatsma, T. P., van Dam, H. J. J., Wang, D., Nieplocha, J., Apra, E., Windus, T. L., de Jong, W. A. NWChem: a comprehensive and scalable open-source solution for large scale molecular simulations Comput. Phys. Commun. 2010, 181, 1477–1489.

32.   Le Bail, A., Duroy, H. & Fourquet, J. L. Ab-initio structure determination of LiSbWO 6 by X-ray powder diffraction Mater. Res. Bull. 1988, 23, 447–452.